Supporting Information for

Generalised level anticrossings explain improved ^{19}F SABRE hyperpolarisation under oscillating magnetic fields

Joni Eronen,* Perttu Hilla, Vladimir V. Zhivonitko, Juha Vaara and Anu M. Kantola*

NMR Research Unit, University of Oulu, P.O. Box 3000, Oulu, FI-90014, Finland.
*Email: joni.eronen@oulu.fi; anu.kantola@oulu.fi

Contents

List of Figures

List of Tables

S1 Supplementary theoretical analysis

S1.1 Floquet theory

The Hamiltonian in Eq. 15 describes the spin dynamics of the three-spin SABRE system in the interaction frame defined by the time-dependent part of the oscillating magnetic field. When the components of the Fourier expansion of the Hamiltonian, given by Eq. 21, are substituted to the Floquet matrix in Eq. 20, we obtain

$$\tilde{H}_\mathrm{F} = \frac{1}{2}\left[\begin{array}{ccc|cc|cc c}
\ddots & & & & \vdots & & & \\
& a_{z0}-2\omega_p & a_xJ_0\left(\frac{a_{z1}}{\omega_p}\right) & 0 & a_xJ_{-1}\left(\frac{a_{z1}}{\omega_p}\right) & 0 & a_xJ_{-2}\left(\frac{a_{z1}}{\omega_p}\right) & \\
& a_xJ_0\left(\frac{a_{z1}}{\omega_p}\right) & -a_{z0}-2\omega_p & a_xJ_1\left(\frac{a_{z1}}{\omega_p}\right) & 0 & a_xJ_2\left(\frac{a_{z1}}{\omega_p}\right) & 0 & \\
\cline{2-7}
& 0 & a_xJ_1\left(\frac{a_{z1}}{\omega_p}\right) & a_{z0} & a_xJ_0\left(\frac{a_{z1}}{\omega_p}\right) & 0 & a_xJ_{-1}\left(\frac{a_{z1}}{\omega_p}\right) & \\
\cdots & a_xJ_{-1}\left(\frac{a_{z1}}{\omega_p}\right) & 0 & a_xJ_0\left(\frac{a_{z1}}{\omega_p}\right) & -a_{z0} & a_xJ_1\left(\frac{a_{z1}}{\omega_p}\right) & 0 & \cdots \\
\cline{2-7}
& 0 & a_xJ_2\left(\frac{a_{z1}}{\omega_p}\right) & 0 & a_xJ_1\left(\frac{a_{z1}}{\omega_p}\right) & a_{z0}+2\omega_p & a_xJ_0\left(\frac{a_{z1}}{\omega_p}\right) & \\
& a_xJ_{-2}\left(\frac{a_{z1}}{\omega_p}\right) & 0 & a_xJ_{-1}\left(\frac{a_{z1}}{\omega_p}\right) & 0 & a_xJ_0\left(\frac{a_{z1}}{\omega_p}\right) & -a_{z0}+2\omega_p & \\
& & & & \vdots & & & \ddots
\end{array}\right]. \tag{S1}$$

S1.2 General periodic polarisation transfer fields

The goal is to define a time-independent, effective Hamiltonian that describes the spin dynamics of a three-spin SABRE system subjected to an oscillating polarisation transfer field. We start by writing the two-state Hamiltonian as in Eq. 13 and replace the sinusoidal modulation with a general time dependence:

$$\begin{aligned} \hat{H} &= a_x\hat{I}_x + [a_{z0} + a_{z1}(t)]\hat{I}_z \\ &= \frac{1}{2}\begin{bmatrix} a_{z0}+a_{z1}(t) & a_x \\ a_x & -a_{z0}-a_{z1}(t) \end{bmatrix}. \end{aligned} \tag{S2}$$

We define an interaction frame using the time-dependent term $a_{z1}(t)\hat{I}_z$ as in ref.[1] and calculate the Hamiltonian that drives the spin dynamics in the interaction frame. The unitary operator is given by

$$\hat{U}_1 = \exp\left[i\hat{I}_z\int_0^t a_{z1}(t')dt'\right], \tag{S3}$$

and the corresponding interaction-frame Hamiltonian reads

$$\begin{aligned} \tilde{H} &= \hat{U}_1\hat{H}\hat{U}_1^\dagger + i\frac{d\hat{U}_1}{dt}\hat{U}_1^\dagger \\ &= \frac{1}{2}\begin{bmatrix} a_{z0} & a_x\exp\left[i\int_0^t a_{z1}(t')dt'\right] \\ * & -a_{z0} \end{bmatrix}. \end{aligned} \tag{S4}$$

Consider the integral $\int_0^t a_{z1}(t')dt'$ in Eq. S4. Because $a_{z1}(t')$ represents the time-dependent part of a waveform with a zero time average, the integral of $a_{z1}(t')$ is periodic. In addition, the exponential of a periodic function is also periodic. Therefore, the Hamiltonian given in Eq. S4 can, in principle, be decomposed into Fourier series. Consequently, we could write the Floquet matrix using the expression given in Eq. 20 which suggests the same resonance condition for an arbitrary waveform as for a sinusoidal field. Inspired by this, we perform the same second interaction frame transformation as described in the main text. An integer m is chosen such that $|a_{z0} + m\omega_p|$ is minimised and the unitary operator of interest is

$$\hat{U}_2 = \exp\left(-i\hat{I}_z m\omega_p t\right). \tag{S5}$$

The second interaction frame Hamiltonian is given by

$$\begin{aligned}\tilde{\tilde{H}} &= \hat{U}_2\tilde{H}\hat{U}_2^\dagger + i\frac{d\hat{U}_2}{dt}\hat{U}_2^\dagger \\ &= \frac{1}{2}\begin{bmatrix} a_{z0} + m\omega_p & a_x \exp\left[i\int_0^t a_{z1}(t')dt' - im\omega_p t\right] \\ * & -a_{z0} - m\omega_p \end{bmatrix}.\end{aligned} \tag{S6}$$

Notice that the above expression is still exact for the two-state model, regardless of the details of the waveform.

S1.3 Square-modulated polarisation transfer fields

Next, we consider a square-modulated polarisation transfer field

$$B_z(t) = \begin{cases} B_0 + B_1, & 0 \le t < T/2 \\ B_0 - B_1, & T/2 \le t < T, \end{cases} \tag{S7}$$

where B_0 is the offset, B_1 the amplitude, and $T = 2\pi/\omega_p$ the period matching to the angular frequency ω_p. In case of a square wave, the time-dependent component $a_{z1}(t)$ can be written as a piecewise function

$$a_{z1}(t) = \begin{cases} a_{z1}, & 0 \le t < T/2 \\ -a_{z1}, & T/2 \le t < T. \end{cases} \tag{S8}$$

Consequently, the Hamiltonian also becomes piecewise constant with the two parts termed A and B in here. Substituting Eq. S8 into Eq. S6 and performing the integral gives

$$\begin{aligned}\tilde{\tilde{H}}_A &= \frac{1}{2}\begin{bmatrix} a_{z0} + m\omega_p & a_x e^{i(a_{z1} - m\omega_p)t} \\ * & -a_{z0} - m\omega_p \end{bmatrix} \\ \tilde{\tilde{H}}_B &= \frac{1}{2}\begin{bmatrix} a_{z0} + m\omega_p & a_x e^{-i(a_{z1} + m\omega_p)t} e^{2\pi i a_{z1}/\omega_p} \\ * & -a_{z0} - m\omega_p \end{bmatrix}.\end{aligned} \tag{S9}$$

We then use the first-order AHT expansion in Eq. 16, which results in

$$\begin{aligned}\tilde{\tilde{H}}_{\text{eff}} &\approx \frac{1}{2\pi/\omega_p}\int_0^{2\pi/\omega_p} \tilde{\tilde{H}} dt \\ &= \frac{1}{2\pi/\omega_p}\left(\int_0^{\pi/\omega_p} \tilde{\tilde{H}}_A dt + \int_{\pi/\omega_p}^{2\pi/\omega_p} \tilde{\tilde{H}}_B dt\right) \\ &= \frac{1}{2}\begin{bmatrix} a_{z0} + m\omega_p & \frac{i a_x a_{z1}\omega_p\left[e^{i\pi\left(m + \frac{a_{z1}}{\omega_p}\right)} - 1\right]}{\pi\left(m^2\omega_p^2 - a_{z1}^2\right)} \\ * & -a_{z0} - m\omega_p \end{bmatrix}.\end{aligned} \tag{S10}$$

There are two special cases in which the denominator in the effective coupling in Eq. S10 becomes zero. First, if $m = 0$, the denominator becomes zero when $a_{z1} = 0$. This means that the amplitude of the square wave is zero, and the effective coupling reduces to a_x, corresponding to the SF-SABRE case. Second, if $m \neq 0$, the denominator becomes zero when $a_{z1} = \pm m\omega_p$. Substituting a_{z1} to Eq. S9 before taking the AHT integral, one finds that the effective coupling reduces to $a_x/2$ in this case.

We perform spin dynamics simulations with the square-modulated fields using the same 3-fluoropyridine example system as in the main text, while otherwise applying the same parameters as for the sinusoidal fields. The resulting time evolution of the state populations is displayed in Fig. S10.

S1.4 Spin systems with multiple heteronuclei of the same type

The theoretical analysis, experiments, and spin dynamics simulations in this work were performed on the 3-fluoropyridine sample, which contains only one ^{19}F nucleus. However, the generalised LAC condition in Eq. 26, as well as the principle of effective coupling, are expected to hold even for systems in which multiple heteronuclei of the same type are within the molecule of interest. This is because the nuclei of the same type are often strongly coupled in the μT-range magnetic fields used in OF-SABRE, which implies that the spin states of the nuclei are changed simultaneously. On the other hand, if the nuclei are far apart and the coupling between them is weak, only the nucleus that is strongly coupled to the hydrides becomes hyperpolarised.

To demonstrate that the presented theory holds for a broader range of spin systems, a coherent spin dynamics simulation was performed on a 3,5-difluoropyridine ligand using a four-spin system that incorporates the hydride protons and the two ^{19}F nuclei from one of the equatorial ligands. The system with the numbering of the spins is shown in Fig. S11A. Experimentally-observed chemical shifts were used: $\delta_1 = \delta_2 = -23.2$ ppm and $\delta_3 = \delta_4 = -124.4$ ppm.[2] The J-couplings were acquired using quantum chemistry: $J_{12} = -7.01$ Hz, $J_{13} = -0.03$ Hz, $J_{23} = 2.44$ Hz, $J_{14} = 0.04$ Hz, $J_{24} = 2.24$ Hz, and $J_{34} = 3.09$ Hz.[3] A cosine-modulated magnetic field was used with the same parameters as for 3-fluoropyridine in the main article: $B_0 = 43.1\ \mu$T, $B_1 = 73.2\ \mu$T, and $T = 10$ ms. The result, shown in Fig. S11B, demonstrates that both ^{19}F nuclei become hyperpolarised similarly to 3-fluoropyridine in Fig. 2.

In addition to the simulation, there exists experimental evidence that OF-SABRE in general is effective when multiple heteronuclei of the same type are present: Nantogma *et al.*[4] have shown that, in the hyperpolarisation of [^{15}N$_3$]-metronidazole, all the ^{15}N nuclei acquired the same polarisation levels.

S2 Materials and methods

S2.1 Experimental details

Sample preparation

Samples were prepared by dissolving 0.5 mM SABRE-precatalyst IrCl(COD)IMes and 15 mM 3-fluoropyridine into 600 µl of deuterated methanol. The Ir-precatalyst was synthesised using a method described in the literature.[5] The deuterated methanol and 3-fluoropyridine were purchased from Sigma-Aldrich. The sample was placed into a regularwall 5 mm tube where it was activated and degassed by flowing pH_2 through the solution for 20 min. Due to the gradual evaporation of the solvent over time, three samples were used throughout the study to ensure consistent results across the experiments.

Measurement setup

Experiments were conducted on a SpinSolve 43 MHz (1 T) benchtop spectrometer (Magritek, Aachen, Germany) together with a self-built SABRE system described in our previous work[3] with small modifications. The previous power source was replaced by a TS250-4 amplifier (Accel Instruments, Irvine, CA, USA) that was fed with a signal via the BNC-2110 terminal block (National Instruments, Austin, TX, USA) generated by the PCI-6289 DAQ card (National Instruments, Austin, TX, USA). A pH_2 generator (Bruker, Billerica, MA, USA) supplied high-purity pH_2 (90%) to the system, and the pressure was maintained at 3 bar (absolute). Since the goal was to study the polarisation transfer mechanisms, the flow rate was set to 20 sccm to reduce the evaporation of the solvent. We acknowledge that, by using a faster pH_2 flow, the attainable polarisation levels would have been greater.

Experiment procedure

In each measurement, the sample was was placed inside a mu-metal shield (Magnetic Shield Corp., Bensenville, IL, USA), and the desired polarisation transfer field was set. The pH_2 flow was started from the computer and the sample was bubbled for 30 s. Relatively short bubbling time was chosen to maintain consistency between the experiments by reducing the effects of evaporation. In the build-up time experiments, the duration of the pH_2 flow was systematically varied. The flow was stopped automatically from the computer and, when using oscillating polarisation transfer fields, the field was set to 100 µT. Changing the field before transferring the sample is important, as otherwise the magnetisation is destroyed during the sample transfer. The sample was manually transferred to the spectrometer, where the signal was acquired automatically 4 s after the flow was stopped. While the sample transfer only took approximately 2 s due to the close proximity of the spectrometer, it proved to be beneficial to wait for a short period of time for the sample to stabilise before acquiring the spectrum. After the spectrum was acquired, the sample was subjected to zero-field conditions for a few seconds to destroy the remaining magnetisation before continuing on the next experiment.

The measurement of relaxation times at varying magnetic fields involved one additional step. First, the sample was hyperpolarised as described above. Hyperpolarisation of ^{19}F used the oscillating polarisation transfer field defined by $B_{\text{high}} = 100$ µT, $B_{\text{low}} = -90$ µT, and $\tau_{\text{low}} = \tau_{\text{high}} = 2$ ms, whereas a static field of $B_0 = 2$ mT was used to hyperpolarise the ^{1}H nuclei. Then, once the pH_2 flow was stopped, the magnetic field was simultaneously adjusted to the relaxation field. In each experiment, the sample was subjected to the relaxation field for varying durations, after which it was moved to the spectrometer for signal acquisition.

Data processing

All NMR spectra were processed using NMRGLUE (v. 0.11) package[6] in PYTHON (v. 3.11.9). The processing pipeline involved data truncation, apodisation, zero-filling, Fourier transform, phase correction, baseline correction, and finally peak integration. An example

^{19}F NMR spectrum of SABRE-hyperpolarised 3-fluoropyridine is shown in Fig. S1. Further data processing involving the calculation of polarisation levels and data fitting was performed in EXCEL and ORIGINPRO 2022b.

S2.2 Spin dynamics simulations

Spin dynamics simulations of the SABRE process were performed using SPINGUIN (v. 0.0.1),[7] an in-house developed open-source PYTHON package capable of general liquid-state NMR simulations of large spin systems. The simulations incorporated coherent spin dynamics, relaxation by the Redfield theory,[8–10] as well as non-linear chemical exchange processes, and were performed in Liouville space with state-space truncation methods.[11] Isotropic rotational diffusion of a rigid molecule was used as a dynamical model in the relaxation theory. All calculations were performed on a consumer-grade laptop equipped with an 11th generation Intel i5 processor and 16 GB of DDR4 RAM. The PYTHON scripts are available at Fairdata Etsin[12] and also accessible via the GitHub repository of the project.[13]

In SABRE experiments, the initial state is defined by a very high degree of singlet spin order of the pH_2 gas and a thermal-equilibrium state for the other nuclei. At the low magnetic fields used in SABRE, the thermal polarisation is negligible. Consequently, the unit state was used to approximate the thermal-equilibrium state. The spin purity of the pH_2 gas was assumed to be 100%.

The interplay of spin dynamics and non-linear chemical kinetics was modelled iteratively by performing three distinct operations at each time propagation step which was set equal to one period of the oscillating field:

1. Measure the z-magnetisation of each spin by obtaining the expectation value of $\hat{I}_{zi}$ for each nucleus i from the current Liouville-space density vector.

2. Calculate the effects of chemical exchange to the density vectors corresponding to the exchanging species. The simulations incorporate a correction to the dissociation rates that takes the non-linear effects better into account.[14]

3. Propagate the density vectors forward in time according to the Liouville-von Neumann equation.

These steps were performed subsequently for 30 s, matching the bubbling time used in the experiments. When observing the relaxation after the SABRE hyperpolarisation process, the simulation continued for another 60 s but without incorporating new pH_2 into the system. The spin polarisation level was calculated from the magnetisation using

$$P(\%) = \frac{\langle \hat{I}_z \rangle}{I} \cdot 100\%, \tag{S11}$$

where I is the appropriate spin quantum number ($I = 1/2$ for both ^{1}H and ^{19}F).

The chemical kinetics of SABRE were modelled involving three spin systems undergoing exchange:

1. The SABRE complex (8 spins): The hydride protons + one equatorial 3-fluoropyridine ligand containing ^{19}F, ^{14}N, and four ^{1}H nuclei.

2. The unbound ligand (6 spins): 3-fluoropyridine in solution, with the same nuclei as above.

3. The pH_2 molecule (2 spins): Dissolved parahydrogen in solution.

The simulations incorporated all relevant NMR interactions: bare-nucleus Zeeman interaction, chemical shielding, J-coupling, dipolar coupling, and quadrupole coupling. In addition, scalar relaxation of the second kind was taken into account using an empirical formula.[15] In the calculation of the coherent Hamiltonian, the isotropic shielding constants corresponding to the chemical shifts were obtained from the experiments (except for ^{14}N), whereas the other relevant parameters affecting the Hamiltonian, including J-couplings, molecular coordinates, nuclear shielding tensors, and electric field gradient tensors, were calculated using quantum-chemical methods as described in ref.[3] The parameters are given in Tables S1 to S10 with the labelling of the spins indicated in Fig. S2. For the modelling of relaxation in the SABRE complex and in the free ligand, the isotropic rotational correlation times of $\tau_c(\text{complex}) = 50$ ps and $\tau_c(\text{free}) = 6$ ps were estimated using the molecular geometry and the Stokes-Einstein-Debye relation.[16,17] Dissociation rates of 20 s^{-1} and 2 s^{-1} for the ligands and hydrides, respectively, were used.

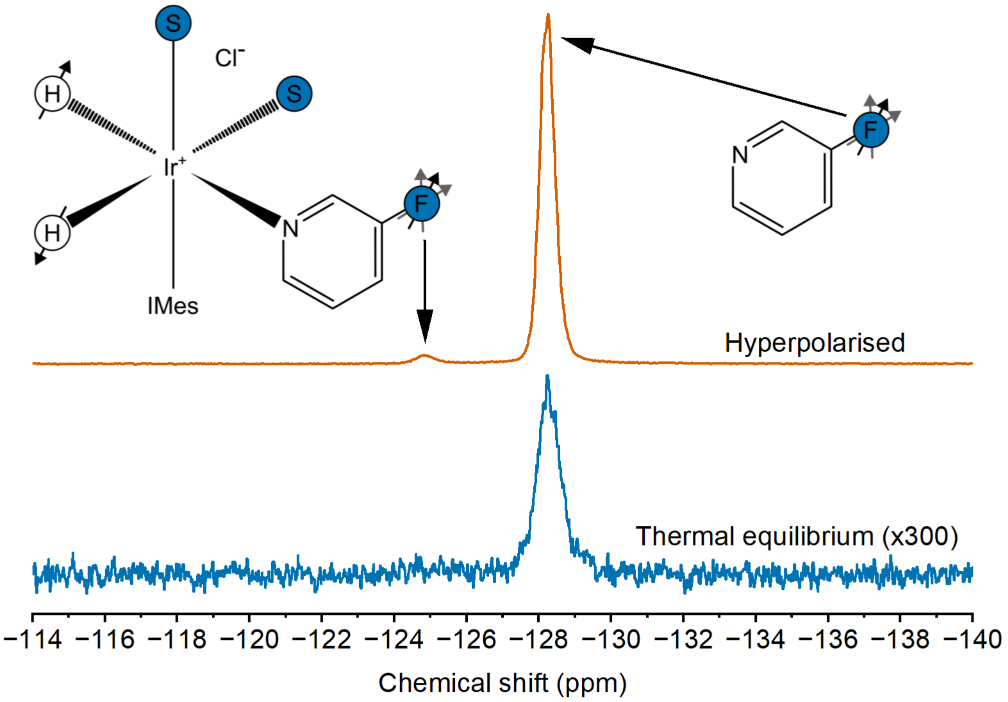

Figure S1: ^{19}F NMR spectra of 3-fluoropyridine SABRE sample. The hyperpolarised spectrum (top) is obtained using OF-SABRE with a bubbling time of 30 s and a square-modulated field: $B_\mathrm{high} = 100\ \mu\mathrm{T}$, $B_\mathrm{low} = -90\ \mu\mathrm{T}$, and $\tau_\mathrm{high} = \tau_\mathrm{low} = 2$ ms. The thermal equilibrium spectrum (bottom) is obtained from an activated SABRE sample in the absence of bubbling. Signals arising from the complex-bound equatorial ligand and the free 3-fluoropyridine in solution are indicated.

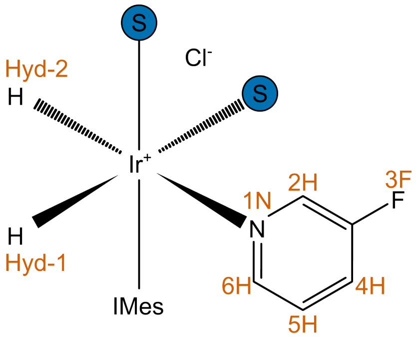

Figure S2: SABRE spin system used in simulations. The atom labels are indicated in orange. Numbering of the free ligand matches the one presented here.

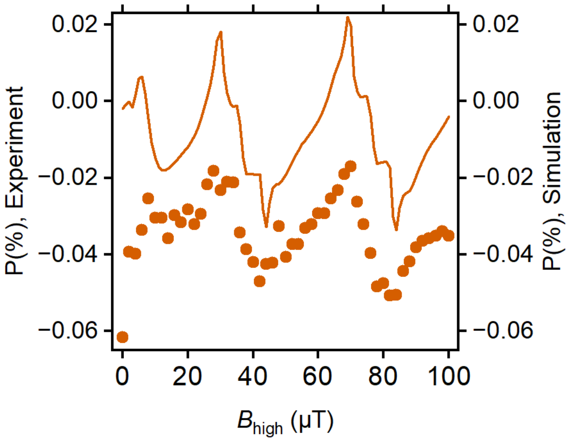

Figure S3: ^{1}H polarisation level with square-modulated polarisation transfer fields as a function of B_{high}. The other field parameters are $B_{\text{low}} = 3$ μT and $\tau_{\text{high}} = \tau_{\text{low}} = 5$ ms. Experimental results (left vertical axis) are shown as symbols and simulations (right vertical axis) as solid line.

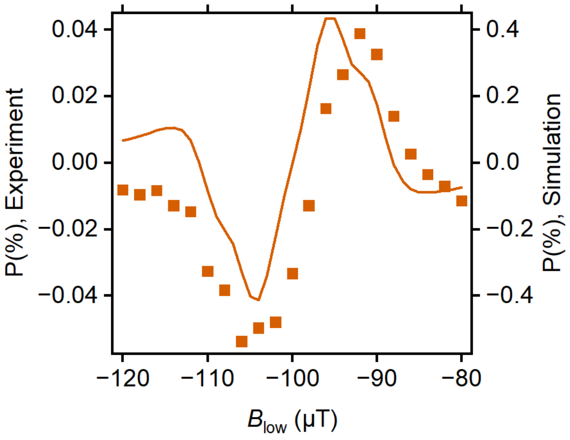

Figure S4: ^{1}H polarisation level with square-modulated polarisation transfer fields as a function of B_{low}. Other field parameters of $B_{\text{high}} = 100$ μT and $\tau_{\text{high}} = \tau_{\text{low}} = 2$ ms, are used. Experimental results (left vertical axis) are shown as symbols and simulations (right vertical axis) as solid line.

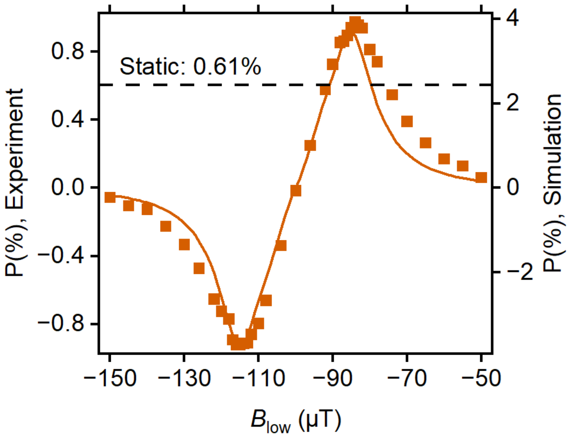

Figure S5: ^{19}F polarisation level with asymmetric rectangular polarisation transfer fields as a function of B_{low}. Other parameters of $B_{\mathrm{high}} = 50$ µT, $\tau_{\mathrm{high}} = 2$ ms, and $\tau_{\mathrm{low}} = 1$ ms, are used. Experimental results (left vertical axis) are shown as symbols and simulations (right vertical axis) as solid line.

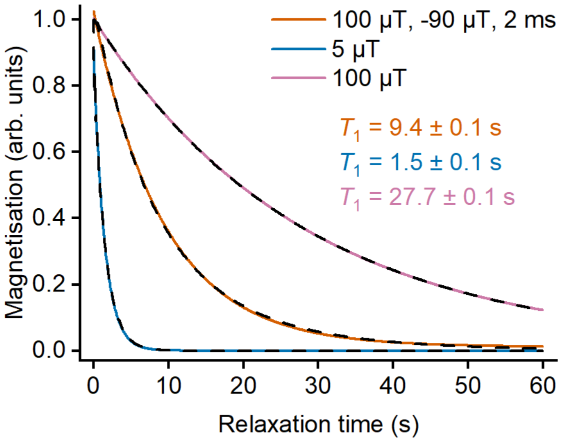

Figure S6: Simulated spin-lattice relaxation of ^{19}F nuclei at selected magnetic fields. Square wave with $B_{\mathrm{high}} = 100$ µT, $B_{\mathrm{low}} = -90$ µT, and $\tau_{\mathrm{high}} = \tau_{\mathrm{low}} = 2$ ms (orange); static 5 µT field (blue); and static 100 µT field (pink). Simulated results are represented by the black dashed lines, and the solid lines show the single-exponential fit, from which the indicated T_1 relaxation times are extracted.

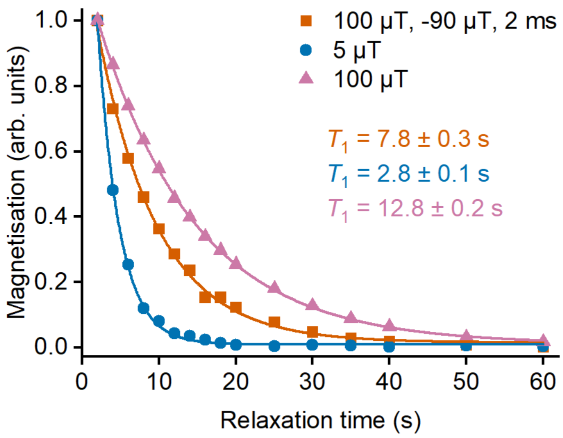

Figure S7: Experimental spin-lattice relaxation of ^{1}H nuclei at selected magnetic fields. Square wave with $B_{\mathrm{high}} = 100$ µT, $B_{\mathrm{low}} = -90$ µT, and $\tau_{\mathrm{high}} = \tau_{\mathrm{low}} = 2$ ms (orange squares); static 5 µT field (blue circles); and static 100 µT field (pink triangles). Solid lines show the exponential fit, from which the indicated T_1 relaxation times are extracted.

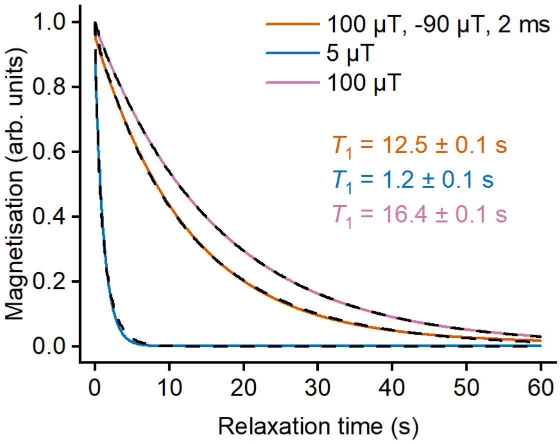

Figure S8: Simulated spin-lattice relaxation of ^{1}H nuclei at selected magnetic fields. Square wave with $B_{\mathrm{high}} = 100$ µT, $B_{\mathrm{low}} = -90$ µT, and $\tau_{\mathrm{high}} = \tau_{\mathrm{low}} = 2$ ms (orange); static 5 µT field (blue); and static 100 µT field (pink). Simulated results are represented by the black dashed lines, and the solid lines show the single-exponential fit, from which the indicated T_1 relaxation times are extracted.

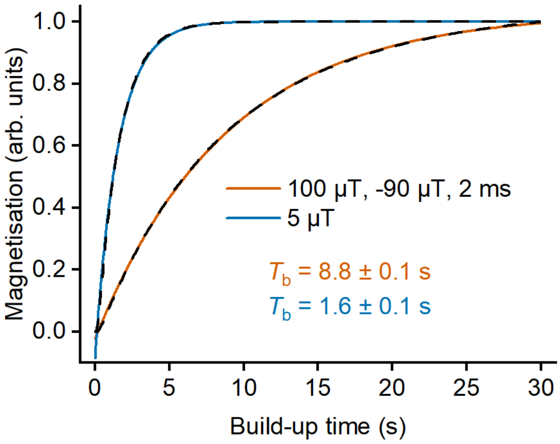

Figure S9: Simulated build-up of ^{19}F spin polarisation at selected magnetic fields. Square wave with $B_{\text{high}} = 100$ µT, $B_{\text{low}} = -90$ µT, and $\tau_{\text{high}} = \tau_{\text{low}} = 2$ ms (orange); static 5 µT field (blue). Simulated results are represented by the black dashed lines, and the solid lines show the single-exponential fit, from which the indicated build-up times T_b are extracted.

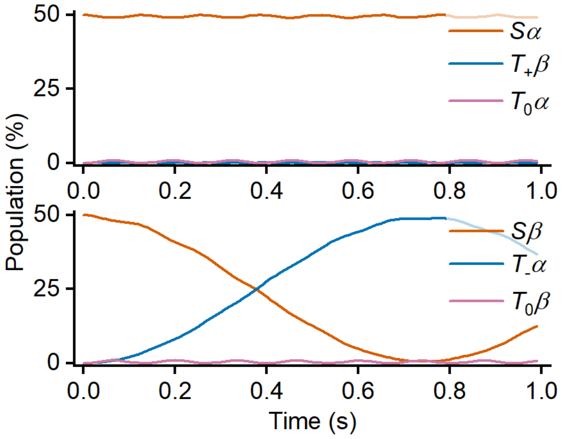

Figure S10: Coherent spin dynamics in OF-SABRE with a square-modulated magnetic field. Numerical simulation of a three-spin system with a field offset $B_0 = 43.1$ µT, an amplitude $B_1 = 73.2$ µT, and a period $T = 10$ ms. The figure shows the time evolution of the populations of each state, starting from equal populations of $|S\alpha\rangle$ and $|S\beta\rangle$.

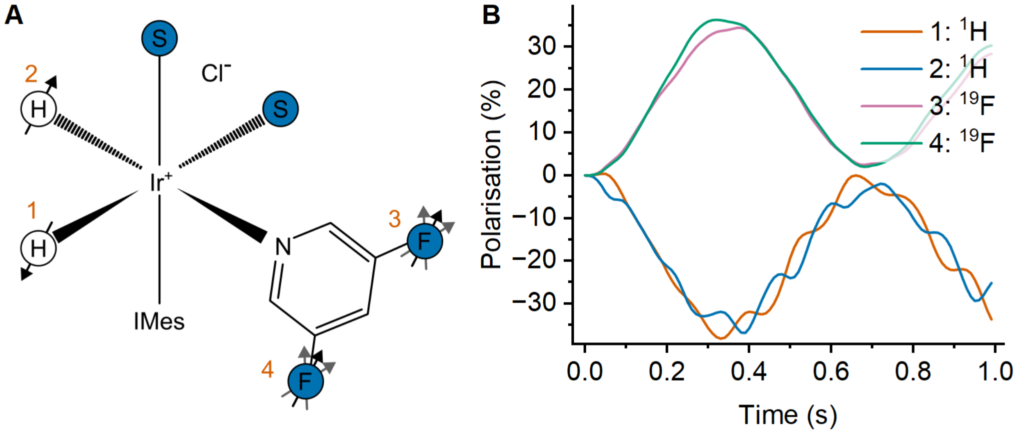

Figure S11: OF-SABRE of a four-spin 3,5-difluoropyridine system. (A) Four-spin system used in the simulations with the numbering of the spins indicated. (B) Spin polarisation acquired from a coherent spin dynamics simulation of OF-SABRE with a cosine-modulated magnetic field. The magnetic-field parameters are: offset $B_0 = 43.1$ µT, amplitude $B_1 = 73.2$ µT, and period $T = 10$ ms. The initial state in the simulations is a singlet state for the hydrides.

Table S1: Isotropic chemical shifts (in ppm) for the SABRE complex.

Hyd-1	Hyd-2	3F	2H	4H	5H	6H	1N
-23.1	-23.1	-124.2	8.38	7.60	7.35	8.04	50.40

Table S2: Isotropic chemical shifts (in ppm) for 3-fluoropyridine.

3F	2H	4H	5H	6H	1N
-127.6	8.49	7.68	7.51	8.43	103.58

Table S3: Scalar *J*-couplings (in Hz) for the SABRE complex.

	Hyd-1	Hyd-2	3F	2H	4H	5H	6H	1N
Hyd-1								
Hyd-2	-7.67							
3F	-0.05	2.08						
2H	-0.03	1.77	1.34					
4H	0.02	0.01	5.69	2.32				
5H	-0.02	0.45	5.07	0.62	8.76			
6H	-0.10	1.49	-0.12	-0.31	0.70	5.80		
1N	-0.23	16.49	-3.56	4.42	-0.32	2.11	4.76	

Table S4: Scalar *J*-couplings (in Hz) for 3-fluoropyridine.

	3F	2H	4H	5H	6H	1N
3F						
2H	-1.21					
4H	7.03	2.46				
5H	4.24	0.70	8.41			
6H	1.17	-1.23	0.73	4.64		
1N	-4.19	7.76	-0.03	0.97	8.48	

Table S5: Molecular coordinates for the SABRE complex.

Atom	x (Å)	y (Å)	z (Å)
Hyd-1	0.1398240	1.6439053	-1.3060737
Hyd-2	1.8274179	0.4353038	-0.6527717
3F	-4.5494695	-2.4608498	-1.0762939
2H	-2.2138624	-1.8675030	-0.2265224
4H	-5.3610375	-0.7518480	-2.8760610
5H	-3.9361017	1.2008714	-3.5904467
6H	-1.7070923	1.4960972	-2.5527510
1N	-1.8489176	-0.1574955	-1.3461032

Table S6: Molecular coordinates for 3-fluoropyridine.

Atom	x (Å)	y (Å)	z (Å)
3F	2.54665675	0.30767466	0.00000000
2H	1.48007090	-2.05232769	0.00000000
4H	0.70997716	2.14955842	0.00000000
5H	-1.74802051	1.60519567	0.00000000
6H	-2.43470826	-0.77989700	0.00000000
1N	-0.51981334	-1.51768965	0.00000000

Table S7: Heavy-atom nuclear shielding tensors (in ppm) for the SABRE complex.

Atom	Cartesian shielding tensor (ppm)		
3F	262.43	-19.75	-50.78
	-10.68	317.21	43.52
	-59.04	39.52	317.90
1N	-96.99	-105.30	-118.64
	-111.01	-97.16	230.57
	-125.45	223.11	42.96

Table S8: Heavy-atom nuclear shielding tensors (in ppm) for 3-fluoropyridine.

Atom	Cartesian shielding tensor (ppm)		
3F	301.37	4.52	0.00
	-9.75	240.18	0.00
	0.00	0.00	376.23
1N	-402.74	75.89	0.00
	68.31	-200.44	0.00
	0.00	0.00	292.45

Table S9: Electric field gradient tensor (in atomic units) for ^{14}N in the SABRE complex.

Atom	Cartesian EFG tensor (a.u.)		
1N	-0.490	-0.164	-0.416
	-0.164	0.293	0.058
	-0.416	0.058	0.198

Table S10: Electric field gradient tensor (in atomic units) for ^{14}N in 3-fluoropyridine.

Atom	Cartesian EFG tensor (a.u.)		
1N	0.193	-0.406	0.000
	-0.406	-0.997	0.000
	0.000	0.000	0.805

References

[1] X. Li, J. R. Lindale, S. L. Eriksson and W. S. Warren, *Phys. Chem. Chem. Phys.*, 2022, **24**, 16462–16470.

[2] A. M. Olaru, T. B. R. Robertson, J. S. Lewis, A. Antony, W. Iali, R. E. Mewis and S. B. Duckett, *ChemistryOpen*, 2018, **7**, 97–105.

[3] J. Eronen, S. K.-M. Svensson, N. Hossain, V. V. Zhivonitko, J. Vaara and A. M. Kantola, *Phys. Chem. Chem. Phys.*, 2025, **27**, 13305–13314.

[4] S. Nantogma, S. L. Eriksson, T. Theis, W. S. Warren, B. M. Goodson and E. Y. Chekmenev, *J. Magn. Reson. Open*, 2025, **24**, 100208.

[5] I. Kownacki, M. Kubicki, K. Szubert and B. Marciniec, *J. Organomet. Chem.*, 2008, **693**, 321–328.

[6] J. J. Helmus and C. P. Jaroniec, *J. Biomol. NMR*, 2013, **55**, 355–367.

[7] J. Eronen and P. Hilla, *Spinguin*, `https://github.com/nmroulu/Spinguin`, Accessed: 2025-08-27.

[8] A. G. Redfield, *IBM J. Res. Dev.*, 1957, **1**, 19–31.

[9] M. Goldman, *J. Magn. Reson.*, 2001, **149**, 160–187.

[10] P. Hilla and J. Vaara, *J. Magn. Reson.*, 2025, **372**, 107828.

[11] H. J. Hogben, P. J. Hore and I. Kuprov, *J. Chem. Phys.*, 2010, **132**, 174101.

[12] J. Eronen, *Data repository of the project*, `https://doi.org/10.23729/fd-83ba92b6-9142-3884-a667-7f5791ab0564`.

[13] J. Eronen, *GitHub repository of the project*, `https://github.com/nmroulu/OF-SABRE-Project`, Accessed: 2025-11-12.

[14] J. R. Lindale, S. L. Eriksson, C. P. N. Tanner and W. S. Warren, *Sci. Adv.*, 2020, **6**, eabb6874.

[15] A. Abragam, *The Principles of Nuclear Magnetism*, Clarendon Press, Oxford, 1961.

[16] N. Bloembergen, E. M. Purcell and R. V. Pound, *Phys. Rev.*, 1948, **73**, 679–712.

[17] J. Kowalewski and L. Mäler, *Nuclear Spin Relaxation in Liquids: Theory, Experiments, and Applications (2nd ed.)*, CRC Press, 2017.